



Full length article

Quantitative prediction of Suzuki segregation at stacking faults of the γ' phase in Ni-base superalloys

Longsheng Feng, You Rao, Maryam Ghazisaeidi, Michael J. Mills, Yunzhi Wang*

Department of Materials Science and Engineering, The Ohio State University, 2041 College Road, Columbus, OH 43210, United States

ARTICLE INFO

Article history:

Received 24 March 2020

Revised 18 August 2020

Accepted 21 August 2020

Available online 2 September 2020

Keywords:

Solute segregation

Segregation isotherm

Creep

Stacking fault

ABSTRACT

Recent experiments suggest that Suzuki segregation may play an important role during deformation in Ni-base superalloys at intermediate temperatures. In this study, a segregation isotherm model incorporating segregation enthalpy from *ab initio* calculations is proposed to predict quantitatively solute enrichment at superlattice intrinsic stacking faults (SISF) within the γ' precipitates in Ni-base superalloys. A sublattice model is employed to describe the γ' phase. A strong correlation between segregation enthalpy and solute enrichment is found. Even though the segregation enthalpy is relatively small, the predicted solute enrichment is consistent with experimental observations. The simulation predictions also suggest a strong cross-correlation among different alloying elements. For example, it is found that segregation of Co on the Ni sublattice at the fault draws segregation of Cr that has a positive segregation enthalpy at the fault without the presence of Co. Such quantitative predictions of equilibrium segregation of solutes at stacking faults in γ' precipitates and its effect on the stacking fault energy could aid the investigation of deformation mechanisms and help the design of superalloys.

© 2020 Acta Materialia Inc. Published by Elsevier Ltd. All rights reserved.

1. Introduction

In crystalline solids, solute atoms tend to segregate at extended defects such as dislocations and grain boundaries through chemical and mechanical interactions between the solutes and the defects as well as among the solutes at the defects. Because of its effects on the kinetics of microstructural evolution and mechanisms of plastic deformation at elevated temperatures, solute segregation at extended defects has been a subject of intensive studies [1–4]. For example, solute segregation and segregation transition at grain boundaries and dislocations, and their drag effects on the migration of these defects, have been studied extensively in the literature [5–13].

Solute atoms also segregate at stacking faults, a phenomenon commonly referred to as *Suzuki segregation* [14,15], and alter the stacking fault energy. This is particularly important for understanding the deformation behavior because the change of stacking fault energy will change the dissociation behavior of dislocations and, hence, impact the cross-slip and twinning processes. For high-temperature alloys strengthened by ordered intermetallic phases, the shearing of ordered precipitates is determined by a fine balance among various stacking fault energies at the deformation

temperature, such as the formation of various stacking fault ribbons [16,17]. Suzuki segregation has also been found crucial to the deformation behavior of the so-called high entropy alloys (HEAs) since studies have shown strong dependence between stacking fault energy (and hence dislocation core structure) and local concentration [18–21]. Even though in some cases there is no solute segregation at the dislocation core [18], the local chemical heterogeneity in the stacking fault definitely impacts the stacking fault energy and the dislocation core structure. While extensive experimental and modeling efforts have been made to verify and quantify the Cottrell atmosphere [22] and grain boundary segregation [23], rather limited studies exist in the literature to quantify the Suzuki segregation. Suzuki [14] predicted that solutes would redistribute at stacking faults with a different concentration as compared to that of the bulk. Due to the limitation of experimental measurements at the time, only indirect evidence such as the width of stacking faults and the size of the extended node of a dislocation network were used to prove the existence of Suzuki segregation. After Suzuki's prediction, it was not until 1980s when Herschitz and Seidman [24,25] did a more systematic study for Co–Fe and Co–Nb binary alloys. Integrated Nb and Fe concentration profiles obtained from the field-ion microscope (FIM) analysis indicated segregation of Nb and Fe atoms to the stacking faults. Saka [26] measured the stacking fault width between two dissociated partial dislocations in a Cu–Si alloy and found that the width of the intrinsic stacking fault (ISF) observed in a slowly-cooled sample

* Corresponding author.

E-mail address: wang.363@osu.edu (Y. Wang).

(10 K per day) was much larger than that observed in a furnace-cooled sample, which was attributed to a decrease of the stacking fault energy through Suzuki segregation. With the advance in electron microscopy characterization techniques, direct evidence such as composition profiles across the stacking faults became possible. Kamino et al. [27] directly measured the concentration profile with high resolution TEM/EDX in Cu–Si alloys and Mendis et al. [28] extended the analysis to twin boundaries. Han et al. [29] also observed widening of the stacking fault region between two partial dislocations at higher temperatures in the MP159 superalloy and measured the concentration profile of Mo, Ti and Nb across the stacking fault using high resolution TEM/EDX. The results showed solute enrichment at the stacking fault.

Within the past decade, more advanced atomic level observations were made to further verify and clarify atomic behavior associated with Suzuki segregation. Yang et al. [30] identified the segregation of Zn and Y atoms along the stacking fault in an Mg–Zn–Y alloy. Viswanathan et al. [31] identified Suzuki segregation at superlattice intrinsic stacking faults (SISF) in two Ni-based superalloys. A recent computational study [32] calculated the generalized-stacking-fault (GSF) energy of {111} plane as a function of Co concentration and showed that the SISF energy in (Ni, Co)₃Al system decreases when Co concentration increases, which also indicates the tendency for Co segregation at SISF. A phase transformation from γ' (L1₂, cubic) to χ (D0₁₉, hexagonal) at SISF was later identified [33,34]. Similar segregation phenomenon was observed by Smith et al [35] at superlattice extrinsic stacking faults (SESF) in ME501 superalloys as well. A phase transformation from γ' to η (D0₂₄, hexagonal) was then proposed after comparing the simulated ordered structure with the experimental observation [35]. It was suggested that this diffusion-mediated segregation transition together with the Cottrell atmosphere could prevent the formation of micro-twinning and consequently improve the creep properties of the alloy. Titus et al. [36] found segregation of W atoms and depletion of Al atoms from SISF in Co-based superalloys. Barba et al. [37] reported segregation of Cr and Co at microtwins in single crystal Ni-based superalloys, indicating the importance of segregation to microtwin formation and growth. Similar segregation behavior at microtwin boundaries was found in a polycrystalline Co-based superalloy [38]. Nie et al. [4] found the segregation of Zn and Gd atoms at twin boundaries in a binary Mg–Zn alloy and a ternary Mg–Zn–Gd alloy, which may explain the annealing strengthening found in these alloys.

Despite numerous experimental reports on Suzuki segregation, limited theoretical analyses of the phenomenon are available. In Suzuki's original treatment [14], the equilibrium segregation is determined by having the exchange potential of solutes being the same in the bulk and at the fault,

$$\left(\frac{\partial G^b}{\partial c}\right)_{c=c_1} = \left(\frac{\partial G^f}{\partial c}\right)_{c=c_2} \quad (1)$$

where G^b and G^f are the Gibbs free energies of the bulk phase and the fault “phase” (also a bulk phase but with the same structure as the stacking fault), respectively. Mendis et al. [28] used this method to calculate the equilibrium Si concentration at the intrinsic stacking fault (ISF) in a Cu–Si alloy and compared it with the experimental observations. Significant differences were found between the theory and experiment. It was argued [28] that the discrepancy might have come from the fact that Suzuki's approach considered the bulk and fault as individual phases but it did not consider the role of interfaces between the two phases, which may be important considering the small thickness (fewer than 10 atomic layers) of the “stacking fault phase”. Titus et al. [36] also used this method to calculate the equilibrium W concentration at SISF in a Co–Al–W ternary alloy and also found a discrepancy with

the experiment result. They solved this issue by doing a cluster expansion study with a stacking fault embedded in the matrix. It has been concluded that bulk thermodynamics breaks down when the free energy of the stacking fault phase is described with its bulk counterparts, as is suggested by the results from Mendis as well [28]. This is not surprising since it may not be appropriate to treat the stacking fault as a bulk phase. The use of bulk free energy as the free energy of the “stacking fault phase” also doesn't include the full contribution of the structural and chemical gradient from the interface between the matrix and “stacking fault phase” (e.g., the last two terms of Eq. (19) in Ref. [8]). Another drawback of this approach is that there is no guarantee that one can find a bulk phase that has the same structure as the stacking fault. If the corresponding bulk phase does not exist, the free energy of the fault cannot be obtained. Therefore, there is a compelling interest to treat this problem with different approaches.

From a theoretical perspective, Suzuki segregation should be much weaker as compared to segregation at grain boundaries and Cottrell atmospheres at dislocations because the atomic structures at the stacking faults and in the bulk are much alike. This raises a question as to how much segregation should be expected at a stacking fault. One could also ask if the observed segregation is really in equilibrium or just a temporary enrichment associated with, inter alia, the reordering process proposed to explain the formation of SISF in Ni-base superalloys [37] or a moving Cottrell-atmosphere [44].

In this study, we formulate a quantitative model combining segregation enthalpy calculations from *ab initio* with segregation isotherm to predict equilibrium solute segregation at SISF in Ni-based superalloys. The use of the segregation isotherm avoids the challenges of not having an accurate free energy for the “stacking fault phase”, due either to the lack of a bulk phase that has the same structure as the stacking fault or to the inaccuracy of using the bulk free energy to describe the stacking fault [28,36]. In this model, the stacking fault is treated as an extended defect, just like grain boundaries or dislocations, where atoms have different atomic surroundings (e.g., the coordination number, bond type, bond angle and bond length, etc.) from atoms in the bulk. We also provide a quantitative analysis (i.e., an analytical equation) on the correlation between segregation enthalpy of a stacking fault and equilibrium solute enrichment at the fault. The model can be easily extended to other ordered intermetallic phases.

2. Methodology

2.1. *Ab initio* calculation of segregation enthalpy

We use *ab initio* calculations to compute the segregation enthalpy of Co and Cr to planar faults in Ni₃Al. These calculations are performed using the plane-wave-based density functional theory code VASP [40] with pseudopotentials generated by the projector augmented wave method with the exchange correlation functional treated by Perdew et al. [41] within the generalized gradient approximation. Atomic positions are optimized using a conjugate-gradient algorithm [42], during which the cell size and shape are not allowed to change. A Monkhorst–Pack k-point mesh [43] of $3 \times 3 \times 1$ is used for the integration in the Brillouin zone. A cut-off energy of 350 eV is used for all calculations, which is 30% higher than the highest value specified in the potential files. Electronic and ionic convergence criteria are 10^{-6} eV and 5×10^{-3} eV/Å, respectively.

The interaction energy $\Delta E_{seg}(x)$ is defined as

$$\Delta E_{seg}(x) = E_{fault}^X(x) - E_{bulk}^X \quad (1)$$

where $E_{fault}^X(x)$ is the total energy of the supercell containing solute X at a distance of x from the stacking fault, and E_{bulk}^X is the

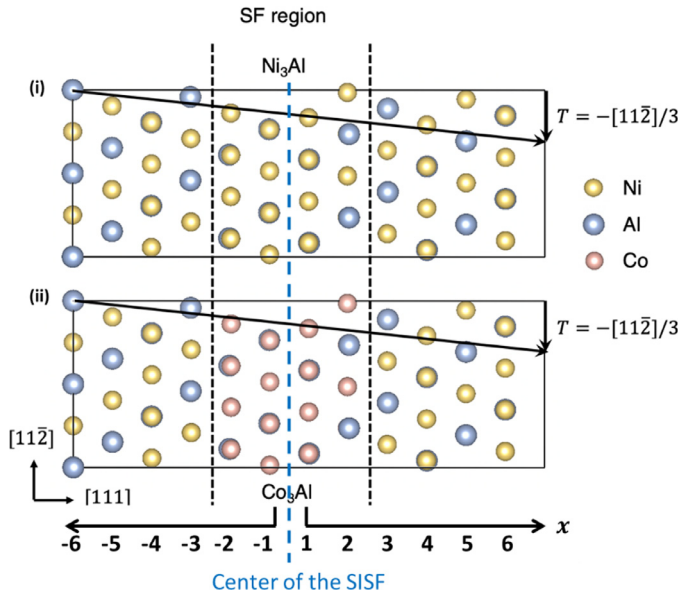


Fig. 1. (a) Simulation cells used in the calculations containing 192 atoms, (i) Ni₃Al and (ii) with Co wetting the stacking fault region. Translation vector $T = -[11\bar{2}]/3$ is used to maintain the periodicity of the cells. The layer numbers show the normalized distance to the stacking fault. Cr atom is introduced to these layers. The center of the SISF (blue dash line) is defined as the center of the SISF region. The distance from layer i to the center of SISF is $(i \pm 0.5) \cdot d_{111}$, the positive sign for $i < 0$ and negative sign for $i > 0$. (b) Stacking sequence difference of {111} planes in γ' (L1₂) and SISF (DO₁₉). (For interpretation of the references to color in this figure legend, the reader is referred to the web version of this article.)

energy of the supercell whose solute X is in the bulk region far from the stacking fault. Fig. 1 shows the structures used in our calculations. The supercell is made of 12 (111) planes of Ni₃Al (L1₂), containing 192 atoms with an area of 87.4 Å². An SISF is created at the center of the cell and a translation vector $\Gamma = -[11\bar{2}]/3$ is applied to the long axis to maintain the periodicity in that direction. The stacking fault (SF) region is defined as the stacking layers that are different from the bulk L1₂ stacking (i.e., ABCABC stacking), which include the ABAB stacking layers (layer 1 and -1) and the interface layers (layer 2 and -2) between the ABCABC stacking and ABAB stacking, following conventions in published literatures [33,36]. To calculate the segregation enthalpy as a function of distance, x , a solute atom (Co or Cr) is introduced to different lattice planes n labeled 1–6 in the figure. We have $x = nd_{111}$ where d_{111} is the interplanar spacing of (111) planes. The synergistic effects between Co and Cr will be investigated by filling the SF region with Co atoms on Ni sublattice, assuming that Co segregates first to the SF. Then the segregation enthalpy for Cr will be calculated using this configuration. This treatment will be discussed later in Section 3 with more details.

2.2. Segregation isotherm

The segregation isotherm at either homo-phase or hetero-phase interfaces is used for calculating the equilibrium solute concentration at stacking faults. For a binary solid solution, the isotherm has the following form [8],

$$\frac{c(x)}{1-c(x)} = \frac{c_0}{1-c_0} \exp\left(-\frac{\Delta F_{seg}(x)}{kT}\right) \quad (2)$$

where $\Delta F_{seg}(x)$ is the free energy of segregation of solutes at interfaces or stacking faults as a function of position, c_0 is the solute concentration in bulk far away from the fault, $c(x)$ is the solute concentration as a function of position away from the fault, k is the Boltzmann constant and T is absolute temperature. When

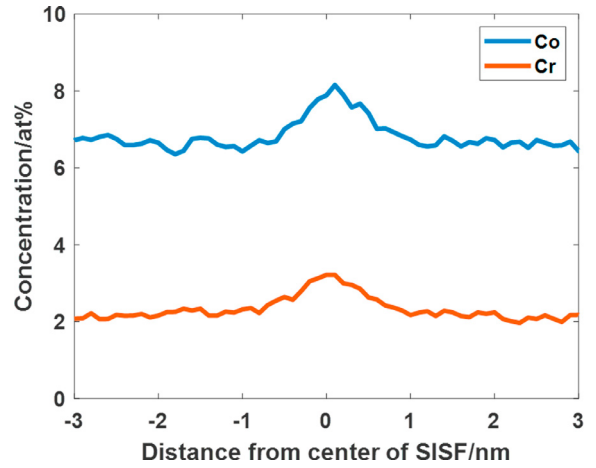


Fig. 2. Co and Cr concentration profile across the SISF in CMSX-4 Ni-based superalloys, adapted from Ref. [31].

the solute is far away from the fault, $\Delta F_{seg}(x)$ approaches zero and $c(x) = c_0$. For dilute solutions (i.e., both c and c_0 are much smaller than 1), if we just consider the solute concentration at the fault, the equation can be reduced to

$$\frac{c_m}{c_0} = \exp\left(-\frac{E_m}{kT}\right) \quad (3)$$

where c_m is the solute concentration at the fault and E_m is the free energy of segregation at the fault. This is the same as Eq. (1) in Cahn's grain boundary segregation model [5].

$\Delta F_{seg}(x)$ usually depends on composition and temperature. In the realm of grain boundary segregation, $\Delta F_{seg}(x)$ has been decomposed into $\Delta H_{seg} - T\Delta S_{seg}$, where ΔH_{seg} is referred to as segregation enthalpy, and ΔS_{seg} is referred to as segregation entropy. At 0 K, the free energy of segregation is equal to segregation enthalpy. It is worth emphasizing that the free energy of segregation accounts for all enthalpic as well as entropic contributions in excess of ideal mixing. If we only consider the configurational entropy of ideal mixing, the free energy of segregation $\Delta F_{seg}(x)$ is just segregation enthalpy ΔH_{seg} . ΔH_{seg} usually has a weak (sometimes negligible) temperature dependence and hence the segregation enthalpy at 0 K is used to compare the magnitude of the free energy of segregation of various solute-defect interactions. The term *interaction energy* is commonly used to describe solute-defect interaction. It does not include solute-solute interaction or solute concentration gradient contribution to the total free energy of segregation. Therefore at 0 K, the interaction energy $\Delta E_{seg}(x)$ in Eq. (1) is approximated to be segregation enthalpy ΔH_{seg} at 0 K in the dilute limit and can be compared with segregation enthalpies of other solute-defect interactions in Fig. 4.

The system we study is a Ni-base superalloy, CMSX-4. The first result of Suzuki segregation in this system was reported by Viswanathan et al. [31] and, from all the elements that were measured, the most prominent segregated species are Co and Cr, which have been proposed to play an important role in the deformation processes [44]. The concentration profile of Co and Cr across an SISF is replotted in Fig. 2 from Fig. 2 in [31]. These two solutes will be considered in this study. Since Ni₃Al is an intermetallic compound, the site occupancy of solutes has to be considered. There have been extensive studies on the site occupancy of solutes in the γ' phase both experimentally and computationally [45–48]. These studies suggest that Co tends to occupy the Ni sublattice [45,46] while Cr tends to occupy the Al sublattice [46–48] in the γ' phase. The site occupancy of solutes on SISF is assumed to be the same as that in the γ' phase (see more discussion in Section 4.7). Therefore, in this study, the segregation behavior of Co and Cr is viewed

as two pseudo-binary systems categorized by sublattices, i.e., Ni-Co system for Co segregation and Al–Cr system for Cr segregation. This assumption follows the *ab initio* calculation of segregation enthalpy in the previous section where the effect of the other sublattice on the segregation enthalpy has been automatically taken into account. Under this assumption, for solutes occupying the Ni sublattice, the maximum solute concentration is 0.75 (0.25 for solutes on the Al sublattice). The free energy of the bulk phase (γ') using the sublattice model [49,50] can be written as

$$G^{\gamma'} = G^{\gamma}(c_i) + G^{\text{order}}(c_i) = G^{\gamma}(c_i) + [\Delta G^{\gamma'}(y_i^{(s)}) - \Delta G^{\gamma'}(y_i^{(s)} = c_i)] \quad (4)$$

$$G^{\gamma}(c_i) = \sum_i c_i G_i^{\gamma} + RT \sum_i c_i \ln c_i + \sum_i \sum_{j \neq i} c_i c_j L_{i,j}^{\gamma} + \sum_i \sum_{j \neq i} \sum_{\substack{k \neq i \\ k \neq j}} c_i c_j c_k L_{i,j,k}^{\gamma} \quad (5)$$

$$\Delta G^{\gamma'}(y_i^{(s)}) = \sum_i \sum_{j \neq i} y_i^{(1)} y_j^{(2)} L_{i,j}^{\gamma'} + RT \left[\frac{3}{4} \sum_i y_i^{(1)} \ln(y_i^{(1)}) + \frac{1}{4} \sum_j y_j^{(2)} \ln(y_j^{(2)}) \right] + \sum_i \sum_{j \neq i} \sum_{\substack{k \neq i \\ k \neq j}} y_i^{(1)} y_j^{(1)} y_k^{(2)} L_{i,j,k}^{\gamma'} + \sum_i \sum_{j \neq i} \sum_{\substack{k \neq i \\ k \neq j}} y_k^{(1)} y_i^{(2)} y_j^{(2)} L_{k,i,j}^{\gamma'} \quad (6)$$

where $G^{\gamma}(c_i)$ and $G^{\text{order}}(c_i) = [\Delta G^{\gamma'}(y_i^{(s)}) - \Delta G^{\gamma'}(y_i^{(s)} = c_i)]$ represent the disordered and ordered branches of the total free energy and $y_i^{(s)}$ is the site fraction of solute i on sublattice s . c_i is the mole fraction of solute i . $L_{i,j}^{\gamma}$ and $L_{i,j,k}^{\gamma}$ are the binary and ternary interaction constants (i.e., regular solution constants) for the disordered solid solution, whereas $L_{i,j}^{\gamma'}$, $L_{i,j,k}^{\gamma'}$ and $L_{k,i,j}^{\gamma'}$ are the interaction constants for the ordered solid solution. In this study, we only consider the zeroth-order interaction terms for the sublattice model since the contributions from higher-order terms are rather small as compared to that of the zeroth-order terms [50]. Without considering antisites, the site fraction ($y_i^{(s)}$) and solute concentration (c_i) follows the relationship given in Table 1. The equilibrium segregation is achieved when the exchange potential is the same ev-

Table 1

Site fraction of Ni, Al, Co and Cr on two sublattices in γ' phase.

	Ni	Al	Co	Cr
Ni sublattice	$\frac{4}{3} c_{\text{Ni}}$	0	$\frac{4}{3} c_{\text{Co}}$	0
Al sublattice	0	$4c_{\text{Al}}$	0	$4c_{\text{Cr}}$

erywhere in the system [8], i.e.,

$$\Delta\mu(\infty) = \Delta\mu(x) \quad (7)$$

where symbol " ∞ " represents a position that is far away from the fault.

The segregation isotherms for Co and Cr segregation can, thus, be expressed by the following equations (see Appendix for details)

$$\frac{c(x)}{0.75 - c(x)} = \frac{c_0}{0.75 - c_0} \exp\left(-\frac{\Delta F_{\text{seg}}(x)}{kT}\right) \quad (8)$$

$$\frac{c(x)}{0.25 - c(x)} = \frac{c_0}{0.25 - c_0} \exp\left(-\frac{\Delta F_{\text{seg}}(x)}{kT}\right) \quad (9)$$

where $\Delta F_{\text{seg}}(x)$ has the form of [8]:

$$\Delta F_{\text{seg}}(x) = E_{\text{int}}(x) + \Delta\mu^{\text{ex}}(c) - \Delta\mu^{\text{ex}}(c_0) - \kappa \frac{d^2 c}{dx^2} \quad (10)$$

where $E_{\text{int}}(x)$ is the segregation enthalpy from the *ab initio* calculations. $\Delta\mu^{\text{ex}}(c)$ is the excess exchange potential beyond an ideal solution. κ is the gradient energy coefficient accounting for the contribution from solute concentration gradient because of the segregation at the fault. According to [8], $\kappa_{\text{Co}} = 0.5A_{\text{Co}}d_{111}^2 = 6.5212 \times 10^{-40} \text{ J} \cdot \text{m}^2/\text{atom}$ and $\kappa_{\text{Cr}} = 0.5A_{\text{Cr}}d_{111}^2 = -3.2420 \times 10^{-39} \text{ J} \cdot \text{m}^2/\text{atom}$. In the current system, the excess exchange potential has the form of

$$\Delta\mu^{\text{ex}}(c_{\text{Co}}) = (0.75 - 2c_{\text{Co}})A_{\text{Co}} \quad (11)$$

$$\Delta\mu^{\text{ex}}(c_{\text{Cr}}) = (0.25 - 2c_{\text{Cr}})A_{\text{Cr}} \quad (12)$$

where A_{Co} and A_{Cr} are interaction constants consisting of various interaction parameters in the sublattice model (see Appendix for details)

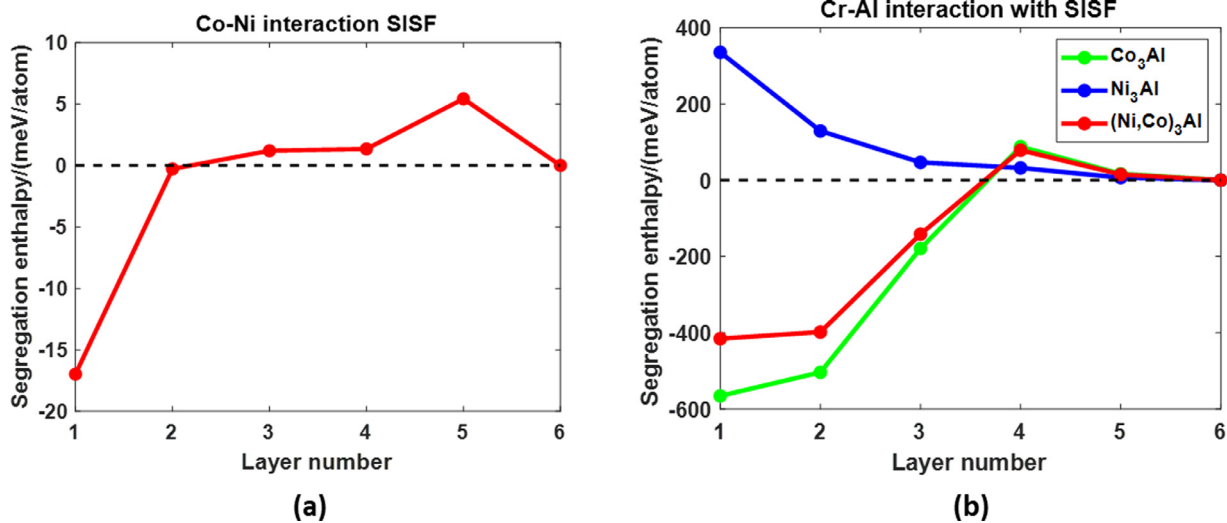


Fig. 3. Segregation enthalpies between (a) Co and SISF, (b) Cr and SISF. The blue curve in Fig. 3(b) titled “Ni₃Al” is the segregation enthalpy for Cr assuming the stacking fault has a chemical constituent of Ni₃Al. The similar is said for the green curve titled “Co₃Al”, details shown in Section 3.2. The red curve is the weighted segregation enthalpy between the blue and green curve with the optimal degree of clustering of Co used to calculate equilibrium Cr segregation in the Co clusters. (For interpretation of the references to color in this figure legend, the reader is referred to the web version of this article.)

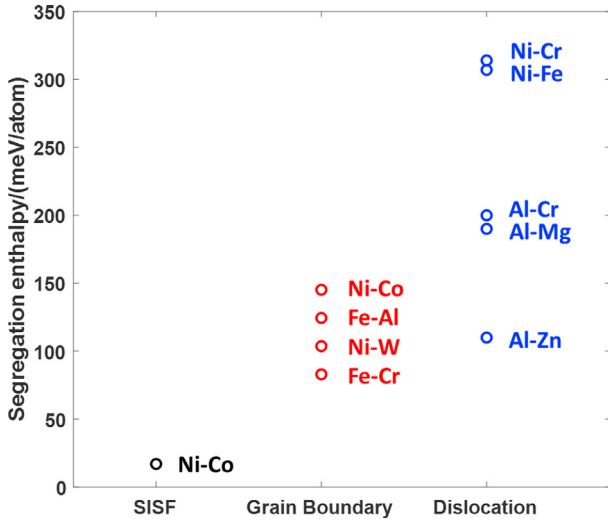


Fig. 4. Magnitude of segregation enthalpy at 0 K (all negative values) of various solute-defect interaction of different metallic alloy systems [51–55].

$$A_{Co} = L_{Ni,Co}^{\gamma} + c_{Cr}L_{Ni,Co,Cr}^{\gamma} + c_{Al}L_{Ni,Co,Al}^{\gamma} + \frac{55}{9} \left(c_{Cr}L_{NiCo,Cr}^{\gamma'} + c_{Al}L_{NiCo,Al}^{\gamma'} \right) \quad (13)$$

$$A_{Cr} = L_{Al,Cr}^{\gamma} + c_{Co}L_{Al,Cr,Co}^{\gamma} + c_{Ni}L_{Al,Cr,Ni}^{\gamma} + \frac{61}{3} \left(c_{Co}L_{Co,AlCr}^{\gamma'} + c_{Ni}L_{Ni,AlCr}^{\gamma'} \right) \quad (14)$$

Eqs. (8) and (9) are used to calculate the equilibrium concentration profile of Co and Cr at SISF. The interaction terms in the sublattice model are taken from [50] and the temperature considered is 750 °C, which is the same as the experimental temperature (Fig. 2) [31].

3. Results

Co and Cr segregation at SISF in the γ' phase of Ni-base superalloys has been widely reported, yet no thermodynamic analysis has been given to rationalize this phenomenon. To understand quantitatively the experimental observations, we first calculated the segregation enthalpy of solutes segregating to SISF and the results are shown in Fig. 3. Note that the result for Co and Cr interacting with SISF in Ni₃Al has been reported in an earlier publication [39]. The negative segregation enthalpy at SISF (inset of Fig. 3(a)) suggests that Co segregation at the fault is expected. The blue curve of Fig. 3(b) shows the segregation enthalpy of Cr at SISF. The positive enthalpy suggests depletion of Cr at the fault, which contradicts to the experiment observation (Fig. 2). In this section we provide quantitative analyses on the equilibrium Co and Cr concentration profiles across an SISF by using segregation isotherm with these segregation enthalpy data obtained from the *ab initio* calculations.

3.1. Equilibrium Co concentration at SISF

Even though the segregation enthalpy at SISF is negative for Co (Fig. 3), its magnitude is rather small as compared to those of grain boundaries and dislocations (see Fig. 4, and detailed discussion in Section 4.1). To understand the relationship between the magnitude of segregation enthalpy and the amount of solute enrichment, we first calculate equilibrium solute enrichment as a function of the magnitude of segregation enthalpy at different temperatures

for a dilute solution using Eq. (3) and compare the results with available experimental data. The results are shown in Fig. 5. The solid lines are the calculation results and the dashed lines indicate the experimental results. For grain boundary segregation in Mg-Gd alloys [51], a solute enrichment of $c_{Co}^{\gamma} = 27$ is observed with a segregation energy of -177 meV at 300 °C (the blue dash line in Fig. 5(a)), which agrees well with the prediction of Eq. (3). The enrichment of Co observed in the experiment (Fig. 2) should correspond to a segregation enthalpy around -20 meV, which is close to what is predicted by the *ab initio* calculation (the black dash line in Fig. 5(b)).

We then use the segregation enthalpy results shown in Fig. 3 to calculate the equilibrium solute concentration profile and compare it with the experimental measurements. The results are presented in Fig. 6(a). The agreement verifies the argument made earlier that even though the segregation enthalpy is small, the solute enrichment is consistent with the experimental measurements. It is also worth noting that the enrichment of Co only appears at the center layers of the fault.

3.2. Equilibrium Cr concentration at SISF

As shown in Fig. 3, Cr has a positive segregation enthalpy at SISF and thus it should be depleted from the SISF if we only consider a Ni–Al–Cr system with Cr occupying the Al sublattice. This is obviously not the case in the experimental observation (Fig. 2). A mechanism on how Cr could diffuse to SISF has been offered [39], but no explanation has been given on what the equilibrium enrichment of Cr should be. We hypothesize that the equilibrium enrichment of Cr is due to the segregation of Co at SISF occupying the Ni sublattice in Ni₃Al. Then the strong Co–Cr nearest neighbor bond will draw Cr to the fault to occupy the Al sites surrounded by Co. To test this hypothesis, we first consider an extreme case where all Ni atoms at the SISF are replaced by Co. The calculated segregation enthalpy $\Delta E_{Cr_{Al}(Co_3Al)}$ of Cr segregating to the SISF is shown by the green curve in Fig. 3(b). The subscript Al in Cr_{Al}(Co₃Al) means Al sublattice and the bracket behind suggests the chemical formula at the fault. The strong negative segregation enthalpy validates our hypothesis. Thus, the Cr–SISF interaction can be viewed as a competition between local depletion due to Cr–Ni₃Al positive interaction and local segregation due to Cr–Co₃Al negative interaction. Thus, Cr clusters at SISF should be expected and this could be validated against future experimental characterization as well.

For the current study, an average segregation enthalpy of Cr as function of Co concentration, $\Delta E_{mix}(c_{Co})$, is estimated by a linear rule-of-mixture of the two segregation enthalpies:

$$\Delta E_{mix}(c_{Co}) = c_{Co}\Delta E_{Cr_{Al}(Co_3Al)} + (1 - c_{Co})\Delta E_{Cr_{Al}(Ni_3Al)} \quad (15)$$

Setting ΔE_{mix} to zero, we obtain a critical uniform Co concentration, 31.25 at%, at the SISF in order to draw Cr to segregate there. Obviously there is insufficient Co to distribute uniformly at the fault to have Cr segregation at the fault in the current system (the Co concentration at the fault ranges from 6% to 20% approximately), but locally, Cr can segregate to Co-rich regions such as Co clusters at the fault (clustering of Co will be discussed in Section 4.4) due to strong Co–Cr bond (discussed in Section 4.5), whereas for the remaining Co-lean regions, Cr will be depleted. However, the overall Cr concentration may still be enriched at the fault. Thus, to predict Cr concentration at the fault based on this hypothesis, we treat the overall Cr concentration at the fault as a weighted average of Cr concentration in these two regions, Ni₃Al, Co-lean and thus Cr-lean, and (Ni, Co)₃Al, Co-rich and thus Cr-rich, with their mole fractions at the fault as the weighting factor, which leads to the following equations

$$x_{Cr} = f x_{Cr,(Ni, Co)_3Al} + (1 - f) x_{Cr,Ni_3Al} \quad (16)$$

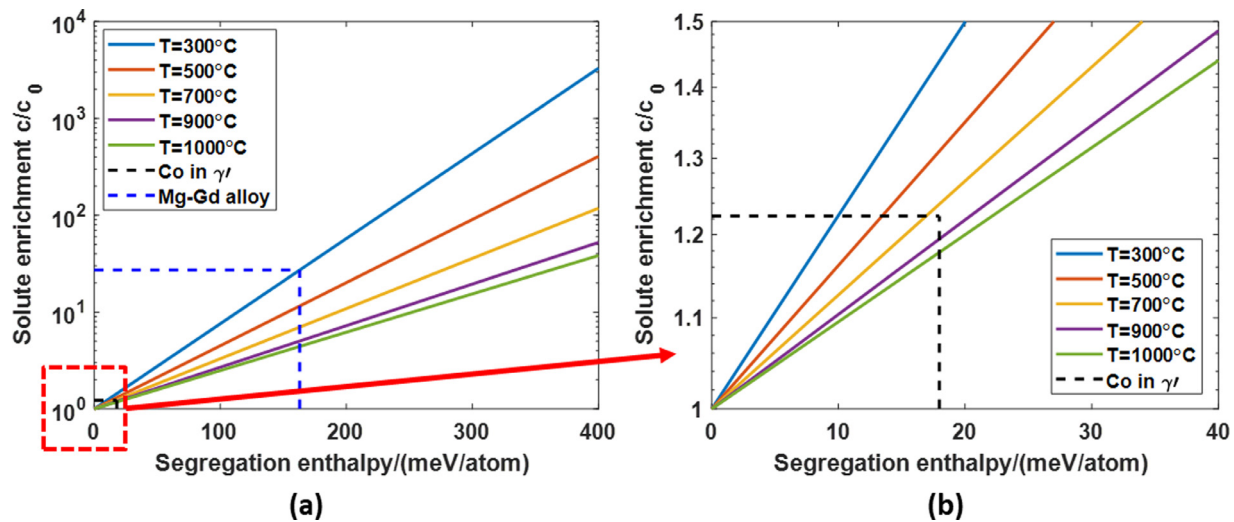


Fig. 5. Correspondence between segregation enthalpy and solute enrichment (log scale) for dilute solutions at various temperatures. The black dash line titled “Co in γ ” is the Co enrichment at SISF shown in Fig. 2 and its corresponding free energy of segregation calculated from Eq. (3). The blue dash line titled “Mg-Gd alloy” is the experimental result of Gd segregation at GB in a Mg-Gd alloy and its corresponding free energy of segregation calculated from Eq. (3). (For interpretation of the references to color in this figure legend, the reader is referred to the web version of this article.)

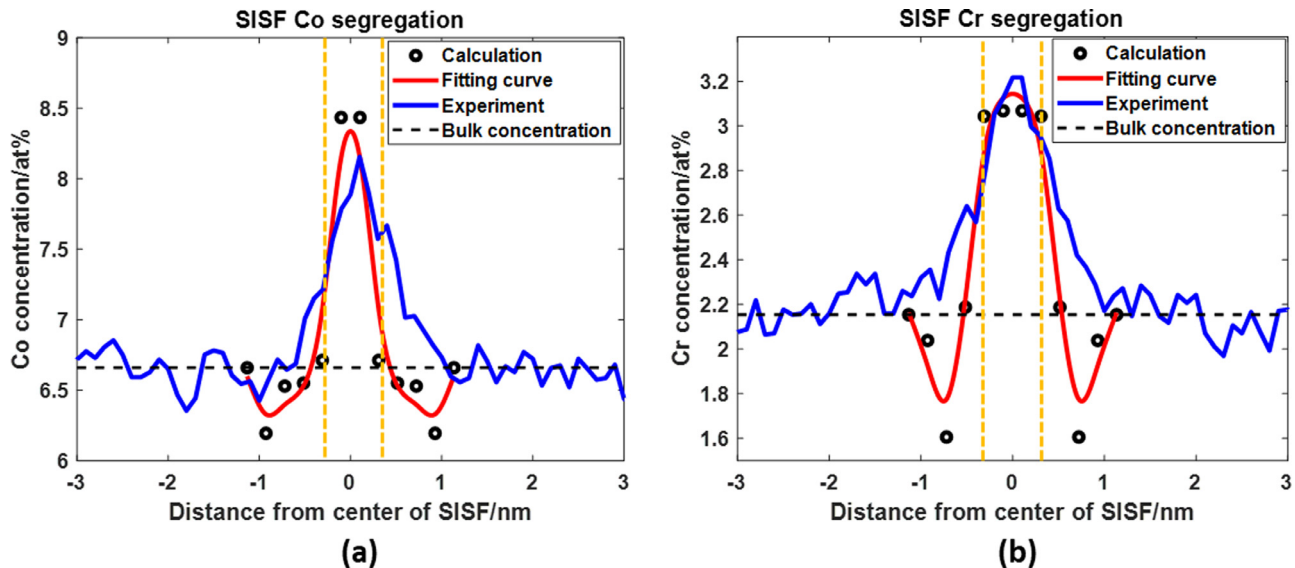


Fig. 6. Concentration profile of (a) Co and (b) Cr across the SISF calculated and compared with the experimental results. The region between vertical oranges dash lines are stacking faults. (For interpretation of the references to color in this figure legend, the reader is referred to the web version of this article.)

$$f \cdot x_{\text{Co}}((\text{Ni}, \text{Co})_3\text{Al}) = x_{\text{Co}}(\text{segregated fault}) \quad (17)$$

where x_{Cr} is the final Cr concentration at the SISF, f is the mole fraction of the Co-rich $(\text{Ni}, \text{Co})_3\text{Al}$ regions, which is defined as the ratio between the total number of atoms in the Co-rich $(\text{Ni}, \text{Co})_3\text{Al}$ regions and total number of atoms at the fault. $x_{\text{Cr}_{-(\text{Ni}, \text{Co})_3\text{Al}}}$ is the Cr concentration at the Co-rich $(\text{Ni}, \text{Co})_3\text{Al}$ regions and $x_{\text{Cr}_{\text{Ni}_3\text{Al}}}$ is the Cr concentration at the Co-lean Ni_3Al regions. $x_{\text{Co}}(\text{segregated fault})$ is the Co concentration at each layer after segregation. Both terms are calculated using Eq. (9) with their own segregation enthalpy. The segregation enthalpy of Cr segregating to Co-lean Ni_3Al regions is the blue curve in Fig. 3(b). The segregation enthalpy of Cr segregating to Co-rich $(\text{Ni}, \text{Co})_3\text{Al}$ regions is still a weighted average using Eq. (15). The higher the Co concentration is in the Co-rich region, the more negative the segregation enthalpy is, and the more enrichment of Cr is in the Co-rich

$(\text{Ni}, \text{Co})_3\text{Al}$ regions (i.e., the higher is $x_{\text{Cr}_{-(\text{Ni}, \text{Co})_3\text{Al}}}$) at the fault. But the Co atoms have to be conserved through Eq. (17). Therefore, the higher is Co concentration in the Co-rich regions, the smaller is the mole fraction, f . Thus, there is an optimal Co concentration in the Co-rich $(\text{Ni}, \text{Co})_3\text{Al}$ regions such that Cr reaches maximum concentration with intermediate values of f and $x_{\text{Cr}_{-(\text{Ni}, \text{Co})_3\text{Al}}}$, and the corresponding segregation enthalpy is plotted as the red curve in Fig. 3(b). The effect of Co concentration in the Co-rich regions is discussed in more detail in Section 4.4.

Fig. 6(b) shows the Cr concentration profile across the SISF calculated in this way. A simple spline fit (the red solid line) is plotted in addition to the discrete data to show the general trend. The peak Cr concentration fits well with the experimental data, which seems to validate our hypothesis. Note that there are valleys in the calculated concentration profiles of Cr (Fig. 6(b)), which are much deeper than the concentration fluctuations in the experiment. This will be discussed in detail in Section 4.5.

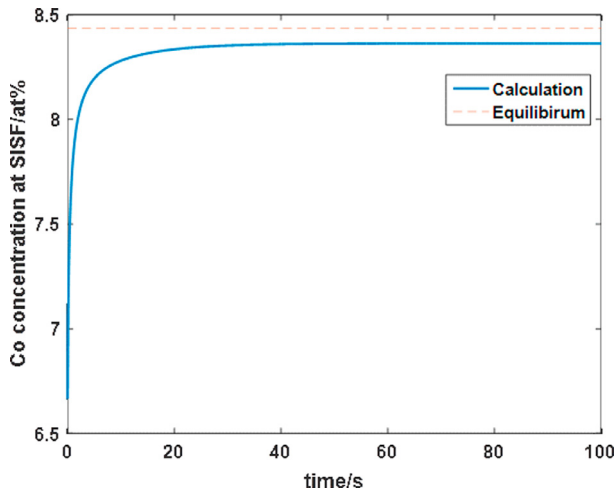


Fig. 7. Co concentration at SISF in CMSX-4 alloy as a function of time through simple solute-SISF interaction at 750 °C.

4. Discussions

4.1. Relation between the value of segregation enthalpy and amount of solute enrichment

Fig. 4 shows a comparison of the calculated segregation enthalpies (magnitude, they are all negative) at different types of extended defects obtained for different binary alloys. In general, solute-dislocation interaction is the strongest due to the large lattice distortion and change of coordination number of atoms at the dislocation core. Depending on atomic size mismatch, the segregation enthalpy magnitude can be up to several hundred meV. Whereas for solute-GB interaction, the segregation enthalpy magnitude is around 100 meV. Solute-SISF segregation enthalpy in the Ni₃Al system is the smallest, with a magnitude less than 50 meV, which suggests the least amount of solute enrichment at SISF. From Figs. 4 and 5, we can come to the following conclusion: for segregation enthalpy magnitude at the level of 10–50 meV, the amount

of solute enrichment at the defect is about a few or a few ten percent (Fig. 4(b)), at various temperatures. This is well aligned with the current calculation results. On the other hand, when the segregation enthalpy magnitude is around one to several hundred meV, the amount of solute enrichment ranges from 10 to 100 times. Therefore, we can conclude that even though the segregation enthalpy for Co at the SISF is relatively small, it is sufficient to give rise to the equilibrium Co enrichment observed in the experiment.

4.2. Time-dependent concentration profile

To verify whether the observed solute concentration at SISF is the equilibrium concentration, the following diffusion equation is solved for a semi-infinite system with a uniform Co concentration at $t=0$,

$$\frac{\partial c}{\partial t} = -\frac{\partial J}{\partial x} \quad (18)$$

where J is the diffusion flux and has the form of [8],

$$J = -c_0(1-c_0)[(1-c_0)m_{Ni} + c_0m_{Co}] \frac{\partial \Delta\mu}{\partial x} \quad (19)$$

where $\Delta\mu$ is the exchange potential of solutes, and m_{Ni} and m_{Co} are the atomic mobilities of Ni and Co in Ni₃Al, respectively. The impurity-diffusivity of Co and self-diffusivity of Ni in Ni₃Al are taken from the CALPHAD database at the experiment temperature (750 °C) [31], $D_{Ni}^* = 3.0 \times 10^{-19} \text{m}^2/\text{s}$ and $D_{Co}^* = 2.1 \times 10^{-19} \text{m}^2/\text{s}$.

Fig. 7 shows the Co concentration at an SISF in CMSX-4 as a function of time. At $t=40$ s, the Co concentration at the SISF has already reached a value that is close to the equilibrium concentration through bulk diffusion. If we consider the Cottrell atmosphere at dislocations and pipe diffusion, the time to reach equilibrium concentration can be even shorter. Compared to the holding time (8 h) in the creep experiment [31], it can be therefore concluded that the Co concentration observed in the experiment has reached equilibrium.

4.3. Effect of solution model

In this study, we only consider 4 atomic species, Ni, Al, Co and Cr. For multicomponent alloys, multiple atomic species exist on

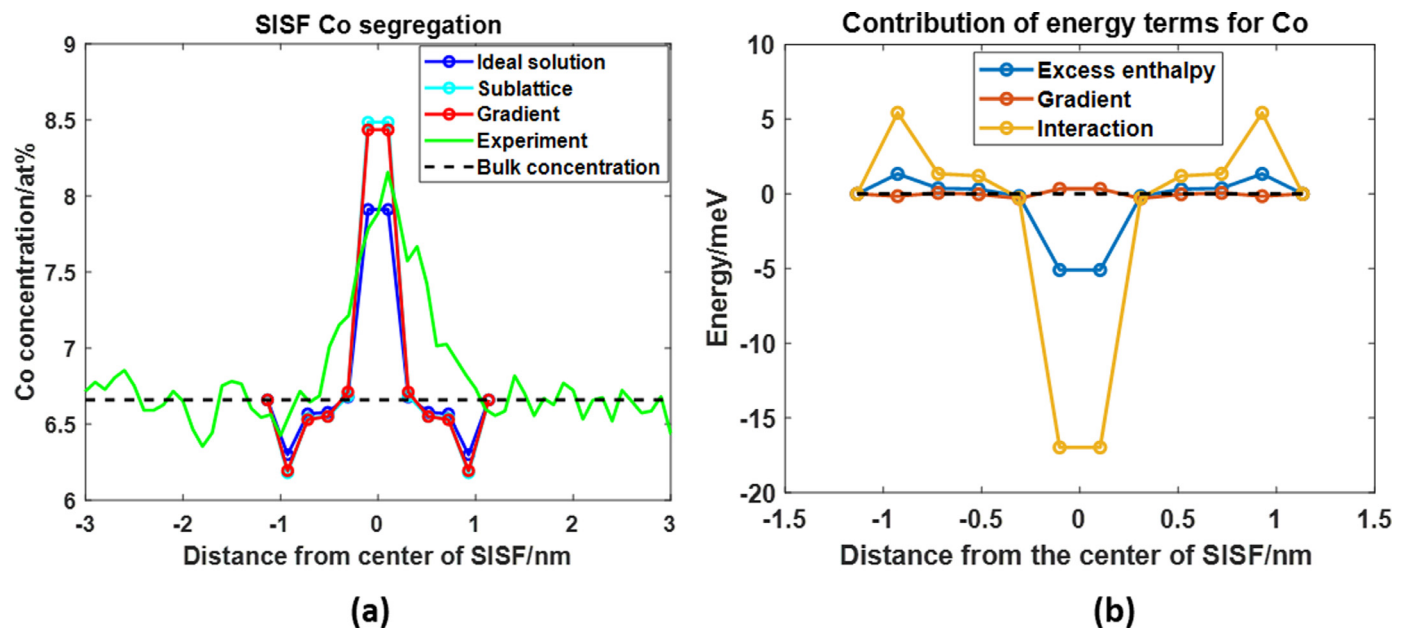


Fig. 8. (a) Co concentration profile for considering different contributions to the segregation energy. (b) Contribution of each term in the segregation energy. (For interpretation of the references to color in this figure, the reader is referred to the web version of this article.)

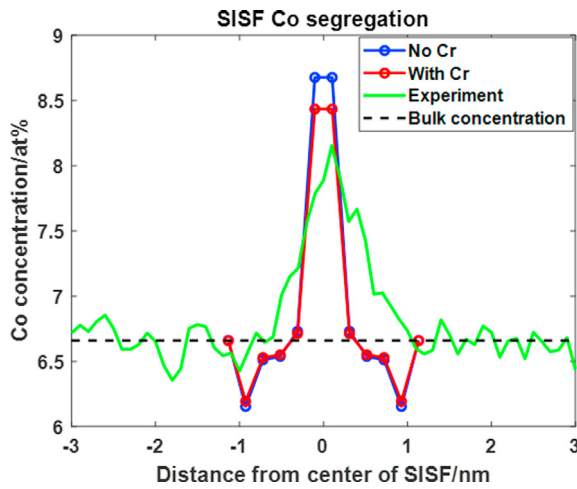


Fig. 9. Effect of Cr on Co concentration profile across the SISF.

specific sublattices. Vacancies and anti-site defects may also exist. In principle, all possible solutes such as Ti, W, Nb, Ta and vacancies could be considered in this model by fixing site fraction of each species and adding more terms in the excess exchange potential term. To gain a better idea on how these factors play a role, we need to understand how each energy term contributes to the segregation profile. Fig. 8(a) shows the Co concentrations with only solute-SISF interaction (the blue curve), with the addition of the excess exchange potential in the sublattice model (the cyan curve), and with the addition of the gradient term (the red curve). Meanwhile, Fig. 8(b) shows the contributions from each of these energy terms. For Co segregation, the main contribution to the segregation energy is still the segregation enthalpy, namely the Co-SISF interaction. By having a more complicated solution model, there is a nontrivial correction of the results. Unlike the grain boundary segregation where there is a significant solute gradient [8], in this SISF case, the contribution of the Co concentration gradient is minimal due to the low level of solute enrichment.

For the pseudo-binary Ni–Co system considered in the current model, it is assumed that the other sublattice (i.e., the Al sublattice) is occupied by both Al and Cr. Fig. 9 shows the Co concentration profile if we do not consider Cr on the Al sublattice. This is done by making Cr concentration zero in the interaction constant A_{Co} in Eq. (13). The result indicates that Cr reduces the segregation of Co at SISF. But the contribution of the correction is small yet non-trivial as compared to the Co-SISF interaction. But the main contribution is still the Co-SISF interaction.

Similar calculations are performed for Cr segregation (Fig. 10). It is clear that the solution model and gradient term have negligible effect on Cr segregation. This is because we calculate the Cr concentration as the result of a combination of two parts, one for Cr segregating to Co-rich (Ni, Co)₃Al regions and the other for Cr depleting from Co-lean Ni₃Al regions at the fault. For each region, the magnitude of the segregation enthalpy is much larger than contributions from the other factors, for example, both segregation enthalpies have magnitude over 300 meV, as shown in Fig. 3(b). In fact, at the fault, the segregation enthalpy of Cr segregating to Co-rich (Ni, Co)₃Al regions is negative enough that Cr almost replaces all Al atoms in the regions, whereas the segregation enthalpy of Cr segregating to Co-lean Ni₃Al region is positive enough that Cr at SISF almost depletes to none. Therefore, the only dominant factor that controls Cr concentration at the fault is the amount and degree of clustering of Co at the fault, which determines the segregation enthalpy of Cr and Co-rich (Ni, Co)₃Al regions and the mole fraction of Co-rich regions.

4.4. Clustering of Co and segregation of Cr at the fault

As mentioned above, we have hypothesized that Co segregation at SISF and formation of Co-rich (Ni, Co)₃Al regions at the fault is responsible for Cr segregation at the fault observed in the experiment. *Ab initio* calculations are performed to verify this hypothesis. Fig. 11 shows the energy difference between two-separate and two-clustered Co atoms in the bulk and at the fault. The results indicate that Co does have a tendency to cluster both in the bulk and at the fault. To describe the clustering behavior in the fault, we introduce a parameter, the degree of clustering, $\eta_{cluster}$, like the short-range order parameter [52], given by the following equation

$$\eta_{cluster} = \frac{P_{CoAl} - P_{CoAl}(average)}{P_{CoAl}(max) - P_{CoAl}(average)} \quad (20)$$

where P_{CoAl} is the probability of finding a Co–Al bond in a Co cluster with the requirement that Co and Al occupy the Ni- and Al-sublattice, respectively. $P_{CoAl}(average)$ is the reference probability for finding a Co–Al bond at the fault if Co is uniformly distributed. When all the Ni sites in Ni₃Al are occupied by Co, Co reaches the highest level of clustering and, therefore, $\eta_{cluster} = 1$. If the chances of finding a Co–Al bond in the cluster is the same as that at the fault with uniform Co distribution, then there is no clustering of Co at the fault. Thus, $\eta_{cluster}$ characterizes the deviation from uniform spatial distribution of Co atoms within the first coordination shell of Al atoms (i.e., on the Ni-sublattice of Ni₃Al) at the fault planes, i.e., the degree of Co clustering at the fault. The effect of the clustering parameter on Cr concentration at SISF is shown in Fig. 12.

Under the fixed numbers of Co atoms at each atomic plane within the fault (determined by the segregation enthalpy of Co at the fault), there is an optimal degree of clustering of Co, i.e., 10 out of 12 sites in the first nearest neighbor coordination shell of an Al atom at the fault are occupied by Co (only two are occupied by Ni) for maximum Cr segregation, which is used in the calculation of the equilibrium Cr segregation (Fig. 6(b)). This calculated Cr concentration profile matches the experimental results.

It is worth noting that if the degree of clustering of Co is far below the critical one, there will be Cr depletion rather than segregation, suggesting that it is possible to have just Co enrichment at SISF but not Cr. At the optimal Co concentration, i.e., 10 out of 12 of the Ni sites in Ni₃Al are occupied by Co, which yields a Co concentration of 62.5 at%, the Cr concentration in the Co clusters will reach 22.73%, which is close to the total Al site fraction (25%). This suggests that the attraction between Cr and Co clusters are so strong that almost all the Al atoms in the clusters tend to be replaced by Cr atoms. The mole fraction of the Co clusters is 13.54% at the optimal degree of clustering calculated from Eq. (17). Due to the nature of Co clustering, the Cr concentration at the fault can be location specific (i.e., different from that in a random L1₂ solid solution).

To better illustrate Co clustering, Fig. 13 shows a schematic of Co cluster (Fig. 13(a) vs random distribution of Co atoms (Fig. 13(b)) on the Ni sublattice on a single {111} plane. Al atom G in Fig. 13(a) is surrounded by 4 Co atoms while all other Al atoms have only 1 (atom B, C, F and H) or 0 (atom A, D and E) Co atom as their first nearest neighbors. From the segregation enthalpy calculations, when Al atom G is swapped with a Cr atom from the bulk, the segregation enthalpy will be negative, while when all other Al atoms are swapped with Cr atoms in the bulk, the segregation enthalpy will be positive. In Fig. 13(b), each Al atom has 1 Co atom as its nearest neighbors. Thus, none of these atoms will be swapped with Cr after Co segregation. The small cluster shown in Fig. 13(a) can further cluster and create even larger concentration modulation within the fault planes. More study is required to understand the size and distributions of these Co clusters.

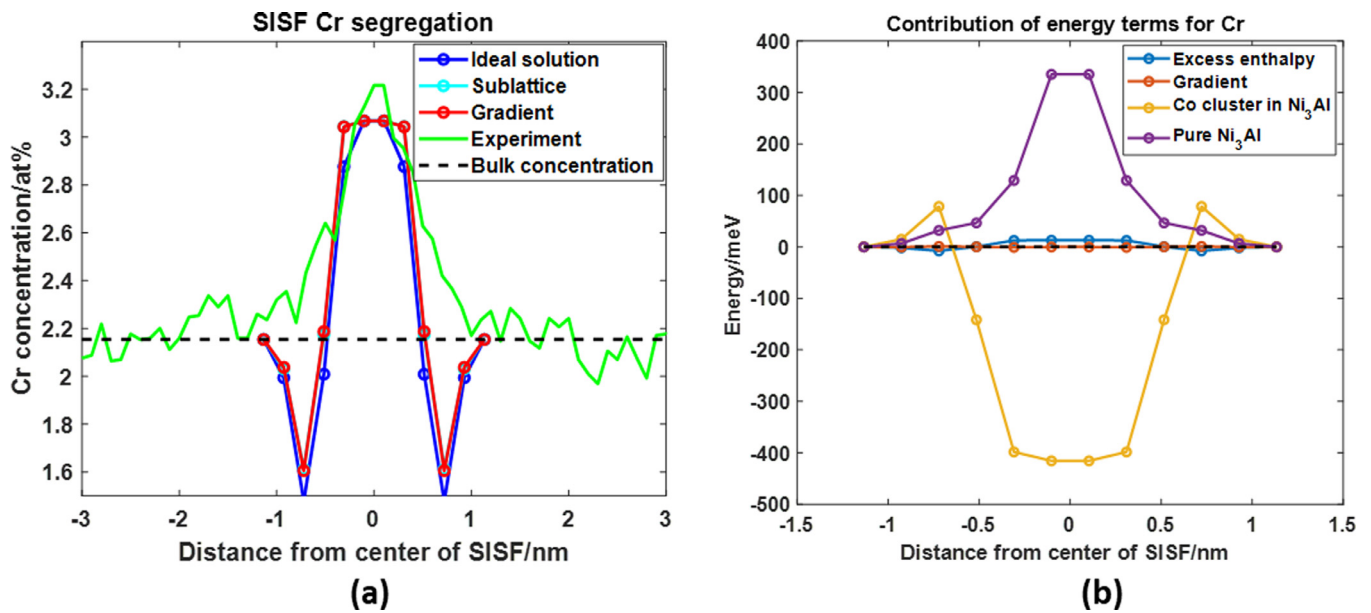


Fig. 10. (a) Cr concentration profile for considering different contributions to the segregation energy. (b) Contribution of each term in the segregation energy.

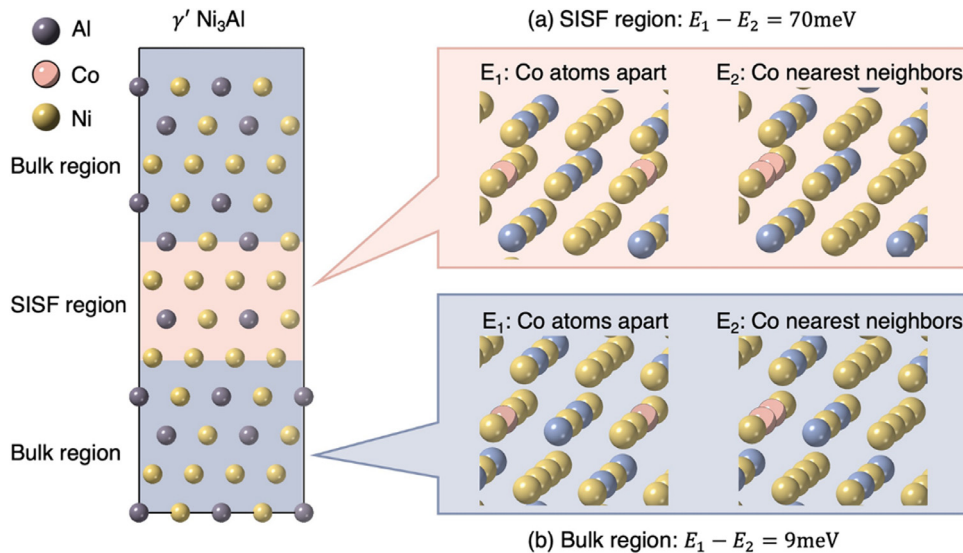


Fig. 11. DFT calculation of the tendency for Co clusters (a) at the SISF and (b) in the bulk. The yellow atoms are Ni, all occupying Ni sites. The pink atoms are Co, also occupying Ni sites. The grey atoms are Al, all occupying Al sites. (For interpretation of the references to color in this figure legend, the reader is referred to the web version of this article.)

4.5. Effects of bonding environment on segregation enthalpy and equilibrium concentration profile

A previous *ab initio* study has concluded [39] that the major reason for segregation at the fault is the enhanced bonding between solutes and their first nearest neighbors. Here we present the charge density difference to illustrate the redistribution of charges during the formation of bonds. An increased density indicates more electrons and thus a stronger bonding. Fig. 14(a) shows the case for an area containing Cr in layer 2 (one layer away from the fault) where the first nearest neighbors of Cr are all Co on this plane (i.e., in the case of Co₃Al). Fig. 14(b) gives the counterpart for Cr in layer 6 (bulk) where the first nearest neighbors are all Ni. It can be seen that more electrons accumulate between Cr and Co as compared to those between Cr and Ni. Therefore, the Cr–Co bonds are stronger than the Cr–Ni bonds and consequently the segregation enthalpy is negative if the segregation process elimi-

nates Cr–Ni bonds and creates Cr–Co bonds. This is why when Co replaces all Ni atoms at the fault, the segregation enthalpy goes from positive to negative (layer 1 of the blue and green curve in Fig. 3(b)).

The change in bonding environment also causes the deep valley in the calculated Cr concentration profile as compared with the experimental measurement in Fig. 6(b). This valley corresponds to the peak of the segregation enthalpy profiles (Fig. 3(b)) at plane 4, which are positive. It is also noted that for both Co₃Al and Ni₃Al regions, the segregation enthalpy at plane 4 is positive. Thus, there will be Cr depletion regardless of the weighting method of the segregation enthalpy between $\Delta E_{\text{CrAl}}(\text{Co}_3\text{Al})$ and $\Delta E_{\text{CrAl}}(\text{Ni}_3\text{Al})$ one chooses. Fig. 14(c) shows the bonding environment of Cr in different planes. As can be seen, from the bulk (layer 6) to the stacking fault (layer 1), the number of Cr–Co bonds increases starting from layer 3, with layer 1 being 100% Cr–Co bonds and layers 4–6 having unchanged number of Cr–Ni bonds. This demonstrates that the

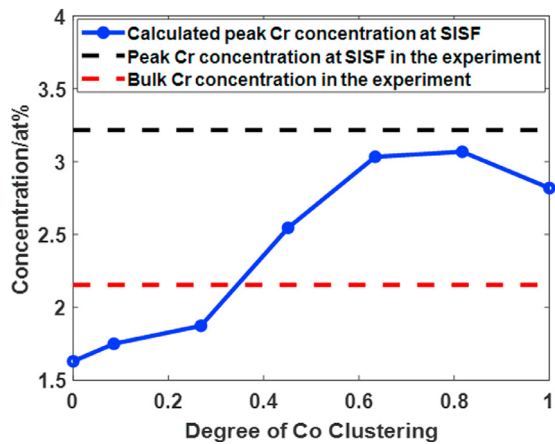


Fig. 12. Effect of Co clustering on Cr concentration at SISF. The bulk Co concentration is 6.66% (black dash line in Fig. 6(a))

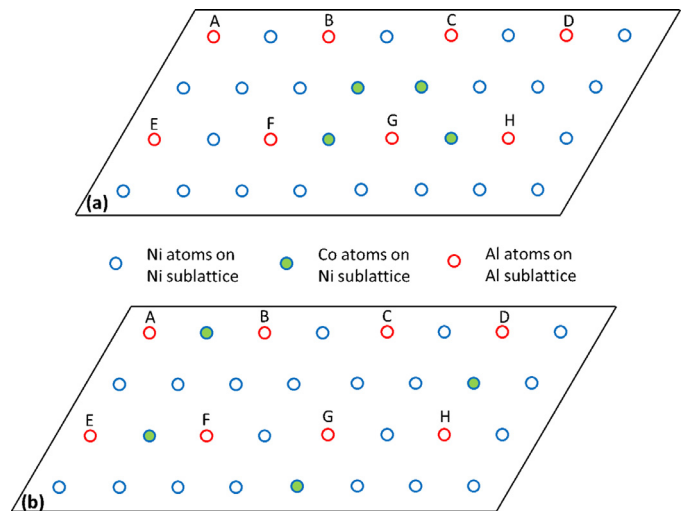


Fig. 13. Schematic demonstration of Co atoms in (a) clusters and (b) random solid solution on Ni sublattice on one {111} plane.

effect of Co on the segregation of Cr in Ni_3Al starts at layer 3 with the largest being at layer 1, while layers 4–6 retain unchanged as compared to that in Ni_3Al . From Fig. 3(b), the segregation enthalpy continuously increases from layer 6 to layer 1 without Co (the blue curve). The addition of Co decreases the values on this curve, but only for layers 3 and below. Therefore, layer 4 remains positive and appears as a peak in the green and red curve in Fig. 3(b). As for the enthalpy itself at layer 4, since we are manually creating another phase Co_3Al at the fault but its lattice constant is kept the same as Ni_3Al , there is more lattice strain in the current configuration. This is an additional contribution to the segregation enthalpy compared to the in Ni_3Al . The effect of the local strain is detailed in the following discussion. This explains the synergistic effect between segregation of Co and Cr.

However, our calculation only takes into account the extreme cases where Co atoms are all restricted to the stacking fault region whereas in experiments, Co will have a broader spatial concentration variation. The local composition and configuration resemble those of Co_3Al at the stacking fault, but in the bulk, there are no Co atoms. This discontinuity in Co concentration gives rise to a mismatch that could cause extra strain energy. Since we only have one solute atom on each lattice plane in the calculations, the effect should be rather local, confined to the vicinity of this solute

Table 2

Local distortion $\bar{\epsilon}$ for Cr in layer 4, 5, and 6.

layer	4	5	6
$\bar{\epsilon}$ (%)	0.53	0.08	0.08

atom. This local distortion can be calculated by

$$\bar{\epsilon} = \frac{1}{n} \sum \frac{|l_i - l_0|}{l_0} \quad (19a)$$

where l_i is the bond length between Cr and its nearest neighbors, l_0 is the average bond length between Al and Ni in a cell without any solutes, and n is the number of nearest neighbors. The quantity $\bar{\epsilon}$ signifies local lattice distortion caused by the substitution of Al with Cr. The results are shown in Table 2. The reason for only considering layers 4–6 is that as shown in Fig. 14(c), other layers have a different bonding environment, and would naturally have a larger distortion. The magnitude of distortion for Cr in layer 4 is several times higher than those in layer 5 or layer 6. This explains the increased positive value for segregation enthalpy observed in layer 4 in Fig. 3(b). Thus, we conclude that this positive segregation enthalpy peak at layer 4 results from the setting of our cal-

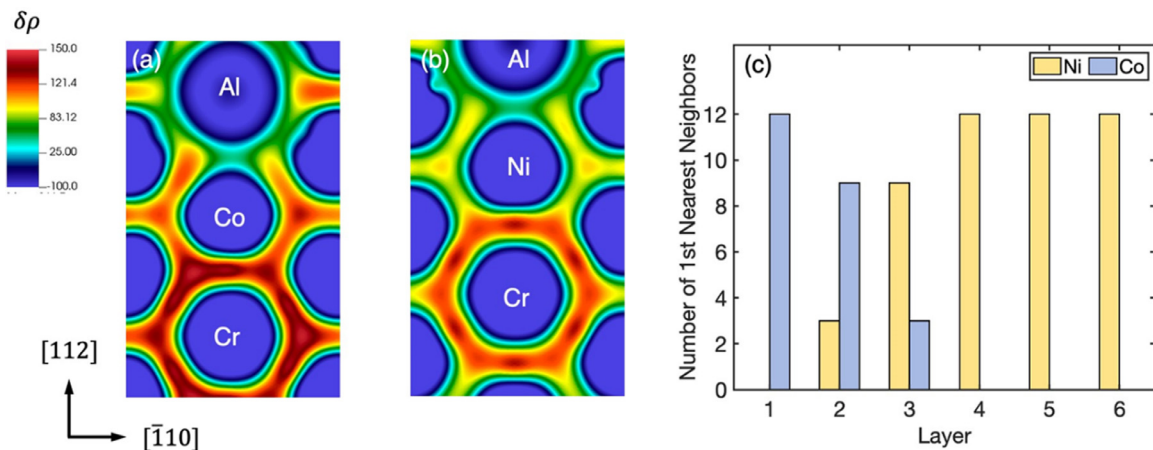


Fig. 14. Charge density difference on (111) planes for an area accommodating the Cr atom. (a) Layer 2, (b) layer 6. (c) shows the bonding environment for the Cr atom on different layers. Ni–Cr bonds switching to Co–Cr bonds can be observed during segregation. The planes 2 and 6 are chosen so that the Cr–Co bonds and Cr–Ni bonds are isolated, and their features are easily seen.

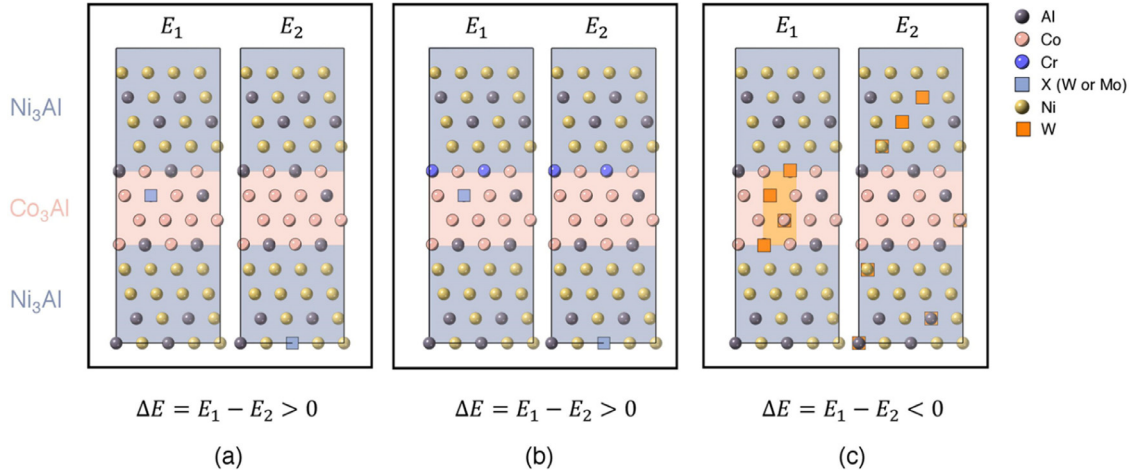


Fig. 15. Segregation enthalpy comparison due to the segregated Co. (a) X (W or Mo) in fault vs in bulk. (b) X in fault vs in bulk with the addition of segregated Cr. (c) W in fault forming Co_3W vs randomly distributed W throughout the cell.

culuation due to limited cell sizes and should not be expected in experiments, as shown in Fig. 6, and that it does not alter our major results on segregation prediction, nor does it signify anything on the deformation mechanisms.

4.6. Effect of Co-segregation on W- and Mo-segregation at SISF

Besides Co and Cr, it has been argued that Mo and W also segregate at SISF in Ni-base superalloys [33]. An unanswered question in [37] is that these solute-SISF interaction energies are all positive, just like Cr, which should result in a depletion of these solutes from the fault whereas the experiment indicates otherwise. Since Cr does segregate at the fault when Co exists at the fault in the system, a similar cross-correlation is possible with respect to Mo and W. *Ab initio* calculations are performed to explore if there exists such a relationship between Co and Mo/W segregation. Fig. 15 shows the schematic illustration and results of the calculations. In the extreme case where all Ni atoms are replaced by Co atoms at SISF, Co does not attract Mo or W to the fault (Fig. 15(a)). Segregation of Cr at SISF does not help to stabilize Mo or W at the fault either (Fig. 15(b)). It can be concluded that Mo and W enrichment may have little to do with the existence and segregation of Co and Cr atoms. However, the energy difference between a uniform distribution of W atoms in the system and concentrated W atoms at the fault does show that W tends to cluster at SISF in Ni_3Al (Fig. 15(c)). This is consistent with the experimental observation of the χ phase (Co_3W) formation at SISF in Ni-based superalloys [33,34]. But what enables this stability is beyond the W-SISF interaction and remains as a puzzle.

4.7. Site occupancy of solutes at SISF

Here, we discuss the site occupancy of solutes at the SISF. The bonding environment for a site in the bulk region and a site in the stacking fault region is the same for up to third nearest neighbors. Therefore, moving from the bulk to the stacking fault, the site preference probably would remain unchanged. Take the site preference of Cr at the stacking fault as an example. First, write the formation energy of Cr replacing Al ($\Delta E(\text{Cr}_{\text{Al}})$) and Ni ($\Delta E(\text{Cr}_{\text{Ni}})$):

$$\Delta E(\text{Cr}_{\text{Al}}) = E(\text{Cr}_{\text{Al}}) - E_0 + \mu_{\text{Al}}^{\gamma'} - \mu_{\text{Cr}}^{\gamma'} \quad (20a)$$

$$\Delta E(\text{Cr}_{\text{Ni}}) = E(\text{Cr}_{\text{Ni}}) - E_0 + \mu_{\text{Ni}}^{\gamma'} - \mu_{\text{Cr}}^{\gamma'} \quad (21)$$

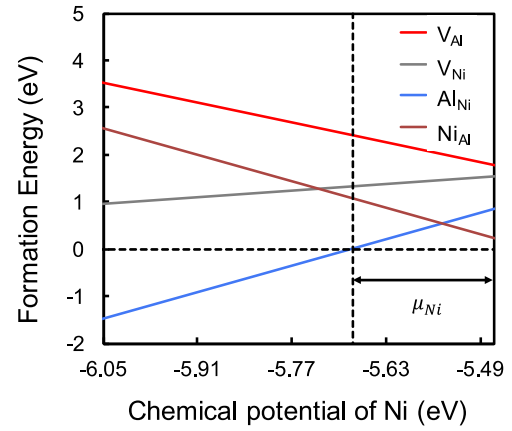


Fig. 16. Formation energies of native point defects in Ni_3Al as a function of chemical potential of Ni. The double arrow indicates allowed Ni chemical potential values.

where $E(\text{Cr}_{\text{Al}})$ is the energy of the cell with a Cr atom on the Al site, E_0 is the energy of pure Ni_3Al , $\mu_{\text{Al}}^{\gamma'}$ and $\mu_{\text{Cr}}^{\gamma'}$ are the chemical potentials of Al and Cr in Ni_3Al , respectively. The subscript Ni denotes the counterparts on Ni site. Now take the difference of the two equations:

$$\Delta E_f^X = \Delta E(\text{Cr}_{\text{Al}}) - \Delta E(\text{Cr}_{\text{Ni}}) = E(\text{Cr}_{\text{Al}}) - E(\text{Cr}_{\text{Ni}}) + \mu_{\text{Al}}^{\gamma'} - \mu_{\text{Ni}}^{\gamma'} \quad (22)$$

If $\Delta E_f^X > 0$, Cr prefers Ni site. Otherwise, Cr prefers Al site. The difficulty is the determination of the chemical potential terms in a compound. Though the absolute values cannot be obtained, the range can be determined by assuming that Ni_3Al is stable at 0 K. This means that all the native point defects should have positive formation energies. For example, we have for an Al vacancy $\Delta E(V_{\text{Al}}) = E(V_{\text{Al}}) - E_0 + \mu_{\text{Al}}^{\gamma'} > 0$. If we also consider the formation energy of Ni vacancy, Al antisite and Ni antisite as a function of $\mu_{\text{Ni}}^{\gamma'}$, we can have the plot shown in Fig. 16. $\mu_{\text{Al}}^{\gamma'}$ and $\mu_{\text{Ni}}^{\gamma'}$ can be interchanged by noticing that $\mu_{\text{Al}}^{\gamma'} + 3\mu_{\text{Ni}}^{\gamma'} = E_0^0$, where E_0^0 is the energy of a perfect Ni_3Al unit cell with 4 atoms. From Fig. 16, we get that the chemical potential range is $-5.679\text{eV} < \mu_{\text{Ni}}^{\gamma'} < -5.465\text{eV}$ and from DFT calculations, we have $E(\text{Cr}_{\text{Al}}) = -1070.188\text{eV}$, $E(\text{Cr}_{\text{Ni}}) = -1069.308\text{eV}$ for a 192-atom cell. Substituting these numbers into Eq. (22) we get $-1.24 < \Delta E_f^X < -0.38\text{eV}$ with the

largest being smaller than zero. This indicates that Cr prefers Al site at the stacking fault region. The same technique can be applied to Co to determine its site preference. Again, the unchanged bonding environment is the major contributing factor for the same site preference for both bulk and stacking fault regions.

4.8. Limitations of the current model

It is assumed in the current model that all the solution constants and gradient terms are layer-independent. This approximation is based on the similar bonding environment of each layer and the lack of accurate thermodynamic data available on the individual layers aside from the bulk. This approximation works in dilute solutions because the contributions of enthalpy of mixing and solute concentration gradient are relatively small as compared to that of the segregation enthalpy. If the model is applied to systems with higher solute concentration like HEAs, the position dependence of solution constants and gradient coefficients have to be considered.

The segregation isotherm is derived under the assumption that the bulk concentration remains constant. The energy $E_{seg}(x)$ from *ab initio* calculation certainly does not satisfy this criterion since there is only one solute atom in the system. Once the solute is swapped from bulk to SISF, the bulk concentration goes to zero. Thus, strictly speaking, $E_{seg}(x)$ from *ab initio* calculation at 0 K is not identical to segregation enthalpy. But in the dilute limit, this variation of bulk concentration will not significantly influence our analysis. However, it is of great importance to explore the effect of bulk concentration variation on $E_{seg}(x)$ such that it can be better incorporated into other alloy systems.

5. Conclusions

A model combining *ab initio* calculations and segregation isotherm is established to quantitatively predict Co and Cr segregation at SISF in Ni-base superalloys. The segregation isotherm is formulated based on the sublattice model and gradient thermodynamics and the segregation enthalpy and clustering tendency of Co is calculated by *ab initio* calculations. The interaction between Co and SISF provides adequate segregation enthalpy (around -20 meV) for Co to reach the amount of enrichment at the fault seen in the experiment. For Cr, our calculations show that, even though Cr has a positive segregation enthalpy at SISF, the segregation of Co atoms stabilizes Cr at SISF, i.e., the segregation of Cr at SISF is caused by a co-segregation effect between Co and Cr. The amount of Cr at SISF depends on the amount and the degree of clustering of Co at SISF in the Ni sublattice (i.e., in the form of $(\text{Ni}, \text{Co})_3\text{Al}$). The enhanced bonding strength between Co and Cr is responsible for the co-segregation effect of Cr and Co. The calculation results provide a quantitative fundamental understanding of the Suzuki segregation phenomenon observed in superalloys and the predictions can also be used to further study the role of solutes in deformation processes in superalloys at elevated temperatures.

Declaration of Competing Interest

The authors declare that they have no known competing financial interests or personal relationships that could have appeared to influence the work reported in this paper.

Acknowledgment

The authors would like to thankfully acknowledge the financial support from NSF DMREF program under grant [DMR-1922239](#).

Appendix

Following Eq. (4), the free energy of the $(\text{Ni}, \text{Co})_3(\text{Al}, \text{Cr})$ system can be written as two parts,

$$G^{\gamma}(c_i) = c_{\text{Ni}}G_{\text{Ni}}^{\gamma} + c_{\text{Al}}G_{\text{Al}}^{\gamma} + c_{\text{Co}}G_{\text{Co}}^{\gamma} + c_{\text{Cr}}G_{\text{Cr}}^{\gamma} \\ + RT[c_{\text{Ni}}\ln(c_{\text{Ni}}) + c_{\text{Al}}\ln(c_{\text{Al}}) + c_{\text{Co}}\ln(c_{\text{Co}}) + c_{\text{Cr}}\ln(c_{\text{Cr}})] \\ + c_{\text{Ni}}c_{\text{Al}}L_{\text{Ni,Al}}^{\gamma} + c_{\text{Ni}}c_{\text{Co}}L_{\text{Ni,Co}}^{\gamma} + c_{\text{Ni}}c_{\text{Cr}}L_{\text{Ni,Cr}}^{\gamma} + c_{\text{Co}}c_{\text{Al}}L_{\text{Co,Al}}^{\gamma} \\ + c_{\text{Co}}c_{\text{Cr}}L_{\text{Co,Cr}}^{\gamma} + c_{\text{Cr}}c_{\text{Al}}L_{\text{Cr,Al}}^{\gamma} + c_{\text{Ni}}c_{\text{Al}}c_{\text{Co}}L_{\text{Ni,Al,Co}}^{\gamma} \\ + c_{\text{Ni}}c_{\text{Al}}c_{\text{Cr}}L_{\text{Ni,Al,Cr}}^{\gamma} + c_{\text{Ni}}c_{\text{Co}}c_{\text{Cr}}L_{\text{Ni,Co,Cr}}^{\gamma} + c_{\text{Co}}c_{\text{Cr}}c_{\text{Al}}L_{\text{Co,Cr,Al}}^{\gamma}$$

and

$$G^{\text{order}}(c_i) = [\Delta G^{\gamma}(y_i^{(s)}) - \Delta G^{\gamma}(y_i^{(s)} = c_i)] \\ = RT\left[\frac{3}{4}y_{\text{Ni}}^{\text{Ni}}\ln(y_{\text{Ni}}^{\text{Ni}}) + \frac{3}{4}y_{\text{Co}}^{\text{Ni}}\ln(y_{\text{Co}}^{\text{Ni}}) + \frac{1}{4}y_{\text{Al}}^{\text{Al}}\ln(y_{\text{Al}}^{\text{Al}}) \right. \\ \left. + \frac{1}{4}y_{\text{Cr}}^{\text{Al}}\ln(y_{\text{Cr}}^{\text{Al}})\right] \\ + y_{\text{Ni}}^{\text{Ni}}y_{\text{Al}}^{\text{Al}}L_{\text{Ni,Al}}^{\gamma'} + y_{\text{Ni}}^{\text{Ni}}y_{\text{Cr}}^{\text{Al}}L_{\text{Ni,Cr}}^{\gamma'} + y_{\text{Co}}^{\text{Ni}}y_{\text{Al}}^{\text{Al}}L_{\text{Co,Al}}^{\gamma'} + y_{\text{Co}}^{\text{Ni}}y_{\text{Cr}}^{\text{Al}}L_{\text{Co,Cr}}^{\gamma'} \\ + y_{\text{Ni}}^{\text{Ni}}y_{\text{Co}}^{\text{Ni}}y_{\text{Al}}^{\text{Al}}L_{\text{Ni,Co,Al}}^{\gamma'} + y_{\text{Ni}}^{\text{Ni}}y_{\text{Co}}^{\text{Ni}}y_{\text{Cr}}^{\text{Al}}L_{\text{Ni,Co,Cr}}^{\gamma'} \\ + y_{\text{Ni}}^{\text{Ni}}y_{\text{Al}}^{\text{Al}}y_{\text{Cr}}^{\text{Al}}L_{\text{Ni,Al,Cr}}^{\gamma'} + y_{\text{Co}}^{\text{Ni}}y_{\text{Al}}^{\text{Al}}y_{\text{Cr}}^{\text{Al}}L_{\text{Co,Al,Cr}}^{\gamma'} \\ - RT\left[\frac{3}{4}c_{\text{Ni}}\ln(c_{\text{Ni}}) + \frac{3}{4}c_{\text{Al}}\ln(c_{\text{Al}}) + \frac{3}{4}c_{\text{Co}}\ln(c_{\text{Co}}) + \frac{3}{4}c_{\text{Cr}}\ln(c_{\text{Cr}}) \right. \\ \left. + \frac{1}{4}c_{\text{Ni}}\ln(c_{\text{Ni}}) + \frac{1}{4}c_{\text{Al}}\ln(c_{\text{Al}}) + \frac{1}{4}c_{\text{Co}}\ln(c_{\text{Co}}) + \frac{1}{4}c_{\text{Cr}}\ln(c_{\text{Cr}})\right] \\ - c_{\text{Ni}}c_{\text{Al}}L_{\text{Ni,Al}}^{\gamma'} - c_{\text{Ni}}c_{\text{Cr}}L_{\text{Ni,Cr}}^{\gamma'} - c_{\text{Co}}c_{\text{Al}}L_{\text{Co,Al}}^{\gamma'} - c_{\text{Co}}c_{\text{Cr}}L_{\text{Co,Cr}}^{\gamma'} \\ - c_{\text{Ni}}c_{\text{Co}}c_{\text{Cr}}L_{\text{Ni,Co,Cr}}^{\gamma'} - c_{\text{Ni}}c_{\text{Co}}c_{\text{Al}}L_{\text{Ni,Co,Al}}^{\gamma'} \\ - c_{\text{Ni}}c_{\text{Al}}c_{\text{Cr}}L_{\text{Ni,Al,Cr}}^{\gamma'} - c_{\text{Co}}c_{\text{Al}}c_{\text{Cr}}L_{\text{Co,Al,Cr}}^{\gamma'}$$

Notice the relationship between $y_i^{(s)}$ and c_i in Table 1.

In addition,

$$c_{\text{Ni}} + c_{\text{Co}} = 0.75 \text{ and } c_{\text{Al}} + c_{\text{Cr}} = 0.25$$

and by applying Eq. (7), Eq. (8)–(14) can be derived.

References

- [1] J.D. Baird, The effects of strain-ageing due to interstitial solutes on the mechanical properties of metals, *Metall. Rev.* 16 (1971) 1–18.
- [2] D. Raabe, M. Herbig, S. Sandl obes, Y. Li, D. Tytko, M. Kuzmina, D. Ponge, P.-P. Choi, Grain boundary segregation engineering in metallic alloys: A pathway to the design of interfaces, *Curr. Opin. Solid State Mater. Sci.* 18 (2014) 253–261.
- [3] A. Yilmaz, The Portevin–Le Chatelier effect: a review of experimental findings, *Sci. Technol. Adv. Mater.* 12 (2011) 063001.
- [4] J.F. Nie, Y.M. Zhu, J.Z. Liu, X.-Y. Fang, Periodic segregation of solute atoms in fully coherent twin boundaries, *Science* 340 (2013) 957–960.
- [5] J.W. Cahn, Critical point wetting, *J. Chem. Phys.* 66 (1977) 3667–3672.
- [6] J.W. Cahn, P. Fife, O. Penrose, A phase-field model for diffusion-induced grain-boundary motion, *Acta Mater.* 45 (1997) 4397–4413.
- [7] M. Kuzmina, M. Herbig, D. Ponge, S. Sandl obes, D. Raabe, Linear complexions: confined chemical and structural states at dislocations, *Science* 349 (2015) 1080–1083.
- [8] N. Ma, S.A. Dregia, Y. Wang, Solute segregation transition and drag force on grain boundaries, *Acta Mater.* 51 (2003) 3687–3700.
- [9] P. Wynblatt, D. Chatain, Solid-state wetting transitions at grain boundaries, *Mater. Sci. Eng.: A* 495 (2008) 119–125.
- [10] N. Ma, C. Shen, S.A. Dregia, Y. Wang, Segregation and wetting transition at dislocations, *Metall. Mater. Trans. A* 37 (2006) 1773–1783.
- [11] S.G. Kim, Y.B. Park, Grain boundary segregation, solute drag and abnormal grain growth, *Acta Mater.* 56 (2008) 3739–3753.
- [12] P.R. Cantwell, M. Tang, S.J. Dillon, J. Luo, G.S. Rohrer, M.P. Harmer, Grain boundary complexions, *Acta Mater.* 62 (2014) 1–48.
- [13] M. Tang, W.C. Carter, R.M. Cannon, Grain boundary transitions in binary alloys, *Phys. Rev. Lett.* 97 (2006) 075502.
- [14] H. Suzuki, Segregation of solute atoms to stacking faults, *J. Phys. Soc. Jpn.* 17 (1962) 322–325.
- [15] H. Suzuki, Chemical interaction of solute atoms with dislocations, *Science Reports of the Research Institutes, Tohoku University, Ser. A Phys. Chem. Metall.* 4 (1952) 455–463.

- [16] C.M.F. Rae, R.C. Reed, Primary creep in single crystal superalloys: origins, mechanisms and effects, *Acta Mater.* 55 (2007) 1067–1081.
- [17] V.A. Vorontsov, L. Kovarik, M.J. Mills, C.M.F. Rae, High-resolution electron microscopy of dislocation ribbons in a CMSX-4 superalloy single crystal, *Acta Mater.* 60 (2012) 4866–4878.
- [18] T.M. Smith, M.S. Hooshmand, B.D. Esser, F. Otto, D.W. McComb, E.P. George, M. Ghazisaeidi, M.J. Mills, Atomic-scale characterization and modeling of 60 dislocations in a high-entropy alloy, *Acta Mater.* 110 (2016) 352–363.
- [19] S.I. Rao, C. Woodward, T.A. Parthasarathy, O. Senkov, Atomistic simulations of dislocation behavior in a model FCC multicomponent concentrated solid solution alloy, *Acta Mater.* 134 (2017) 188–194.
- [20] Y. Zeng, X. Cai, M. Koslowski, Effects of the stacking fault energy fluctuations on the strengthening of alloys, *Acta Mater.* 164 (2019) 1–11.
- [21] R. Zhang, S. Zhao, J. Ding, Y. Chong, T. Jia, C. Ophus, M. Asta, R.O. Ritchie, A.M. Minor, Verification of Short-Range Order and Its Impact on the Properties of the CrCoNi Medium Entropy Alloy, *ArXiv Preprint ArXiv:1912.05610*. (2019).
- [22] A.H. Cottrell, B.A. Bilby, Dislocation theory of yielding and strain ageing of iron, *Proc. Phys. Soc. Sect. A* 62 (1949) 49.
- [23] M.P. Seah, E.D. Hondros, Grain boundary segregation, *Proc. R. Soc. Lond. A Math. Phys. Sci.* 335 (1973) 191–212.
- [24] R. Herschitz, D.N. Seidman, Atomic resolution observations of solute-atom segregation effects and phase transitions in stacking faults in dilute cobalt alloys—I. Experimental results, *Acta Metall.* 33 (1985) 1547–1563.
- [25] R. Herschitz, D.N. Seidman, Atomic resolution observations of solute-atom segregation effects and phase transitions in stacking faults in dilute cobalt alloys—II. Analyses and discussion, *Acta Metall.* 33 (1985) 1565–1576, doi:10.1016/0001-6160(85)90056-2.
- [26] H. Saka, Experimental evidence for Suzuki segregation to the stacking fault of an extended dislocation in a Cu-Si alloy, *Philos. Mag. A* 47 (1983) 131–140.
- [27] T. Kamino, Y. Ueki, H. Hamajima, K. Sasaki, K. Kuroda, H. Saka, Direct evidence for Suzuki segregation obtained by high-resolution analytical electron microscopy, *Philos. Mag. Lett.* 66 (1992) 27–31.
- [28] B.G. Mendis, I.P. Jones, R.E. Smallman, Suzuki segregation in a binary Cu-Si alloy, *Microscopy* 53 (2004) 311–323, doi:10.1093/jmicro/dfh045.
- [29] G.W. Han, I.P. Jones, R.E. Smallman, Direct evidence for Suzuki segregation and Cottrell pinning in MP159 superalloy obtained by FEG(S)TEM/EDX, *Acta Mater.* 51 (2003) 2731–2742, doi:10.1016/S1359-6454(02)00359-2.
- [30] Z. Yang, M.F. Chisholm, G. Duscher, X. Ma, S.J. Pennycook, Direct observation of dislocation dissociation and Suzuki segregation in a Mg-Zn-Y alloy by aberration-corrected scanning transmission electron microscopy, *Acta Mater.* 61 (2013) 350–359, doi:10.1016/j.actamat.2012.09.067.
- [31] G.B. Viswanathan, R. Shi, A. Genc, V.A. Vorontsov, L. Kovarik, C.M.F. Rae, M.J. Mills, Segregation at stacking faults within the γ' phase of two Ni-base superalloys following intermediate temperature creep, *Scr. Mater.* 94 (2015) 5–8.
- [32] J.R. Mianroodi, P. Shanthraj, P. Kontis, J. Cormier, B. Gault, B. Svendsen, D. Raabe, Atomistic phase field chemomechanical modeling of dislocation-solute-precipitate interaction in Ni-Al-Co, *Acta Mater.* 175 (2019) 250–261.
- [33] T.M. Smith, B.D. Esser, B. Good, M.S. Hooshmand, G.B. Viswanathan, C.M.F. Rae, M. Ghazisaeidi, D.W. McComb, M.J. Mills, Segregation and phase transformations along superlattice intrinsic stacking faults in Ni-based superalloys, *Mater. Trans. A* 49 (2018) 4186–4198.
- [34] T.M. Smith, B.S. Good, T.P. Gabb, B.D. Esser, A.J. Egan, L.J. Evans, D.W. McComb, M.J. Mills, Effect of stacking fault segregation and local phase transformations on creep strength in Ni-base superalloys, *Acta Mater.* 172 (2019) 55–65, doi:10.1016/j.actamat.2019.04.038.
- [35] T.M. Smith, B.D. Esser, N. Antolin, G.B. Viswanathan, T. Hanlon, A. Wessman, D. Mourer, W. Windl, D.W. McComb, M.J. Mills, Segregation and η phase formation along stacking faults during creep at intermediate temperatures in a Ni-based superalloy, *Acta Mater.* 100 (2015) 19–31 (1996) 3865–3868, doi:10.1103/PhysRevLett.77.3865.
- [36] M.S. Titus, R.K. Rhein, P.B. Wells, P.C. Dodge, G.B. Viswanathan, M.J. Mills, A. Van der Ven, T.M. Pollock, Solute segregation and deviation from bulk thermodynamics at nanoscale crystalline defects, *Sci. Adv.* 2 (2016) e1601796.
- [37] D. Barba, T.M. Smith, J. Miao, M.J. Mills, R.C. Reed, Segregation-assisted plasticity in Ni-based superalloys, *Metall. Mater. Trans. A* 49 (2018) 4173–4185.
- [38] L.P. Freund, O.M.D.M. Messé, J.S. Barnard, M. Göken, S. Neumeier, C.M.F. Rae, Segregation assisted microtwinning during creep of a polycrystalline L12-hardened Co-base superalloy, *Acta Mater.* 123 (2017) 295–304, doi:10.1016/j.actamat.2016.10.048.
- [39] Y. Rao, T.M. Smith, M.J. Mills, M. Ghazisaeidi, Segregation of alloying elements to planar faults in γ' -Ni3Al, *Acta Mater.* 148 (2018) 173–184, doi:10.1016/j.actamat.2018.01.055.
- [40] G. Kresse, J. Furthmüller, Efficient iterative schemes for ab initio total-energy calculations using a plane-wave basis set, *Phys. Rev. B* 54 (1996) 11169.
- [41] J.P. Perdew, K. Burke, M. Ernzerhof, Generalized gradient approximation made simple, *Phys. Rev. Lett.* 77
- [42] W.H. Press, S.A. Teukolsky, B.P. Flannery, W.T. Vetterling, Numerical Recipes in FORTRAN 77: Volume 1, Volume 1 of Fortran Numerical Recipes: The Art of Scientific Computing, Cambridge University Press, 1992 https://books.google.com/books?id=gn_4mpdN9WkC.
- [43] H.J. Monkhorst, J.D. Pack, Special points for Brillouin-zone integrations, *Phys. Rev. B* 13 (1976) 5188–5192, doi:10.1103/PhysRevB.13.5188.
- [44] T.M. Smith, Y. Rao, Y. Wang, M. Ghazisaeidi, M.J. Mills, Diffusion processes during creep at intermediate temperatures in a Ni-based superalloy, *Acta Mater.* 141 (2017) 261–272.
- [45] M.H.F. Sluiter, Y. Kawazoe, Site preference of ternary additions in Ni_3Al , *Phys. Rev. B* 51 (1995) 4062–4073, doi:10.1103/PhysRevB.51.4062.
- [46] Q. Wu, S. Li, Alloying element additions to Ni3Al: Site preferences and effects on elastic properties from first-principles calculations, *Comput. Mater. Sci.* 53 (2012) 436–443, doi:10.1016/j.commatsci.2011.09.016.
- [47] C. Booth-Morrison, Z. Mao, R.D. Noebe, D.N. Seidman, Chromium and tantalum site substitution patterns in Ni3Al(L12) γ' -precipitates, *Appl. Phys. Lett.* 93 (2008) 033103, doi:10.1063/1.2956398.
- [48] Y. Zhou, Z. Mao, C. Booth-Morrison, D.N. Seidman, The partitioning and site preference of rhenium or ruthenium in model nickel-based superalloys: An atom-probe tomographic and first-principles study, *Appl. Phys. Lett.* 93 (2008) 171905, doi:10.1063/1.2998654.
- [49] N. Dupin, I. Ansara, B. Sundman, Thermodynamic re-assessment of the ternary system Al-Cr-Ni, *Calphad* 25 (2001) 279–298, doi:10.1016/S0364-5916(01)00049-9.
- [50] X.L. Liu, G. Lindwall, T. Gheno, Z.-K. Liu, Thermodynamic modeling of Al-Co-Cr, Al-Co-Ni, Co-Cr-Ni ternary systems towards a description for Al-Co-Cr-Ni, *Calphad* 52 (2016) 125–142, doi:10.1016/j.calphad.2015.12.007.
- [51] I. Basu, K.G. Pradeep, C. Mießen, L.A. Barrales-Mora, T. Al-Samman, The role of atomic scale segregation in designing highly ductile magnesium alloys, *Acta Mater.* 116 (2016) 77–94, doi:10.1016/j.actamat.2016.06.024.
- [52] D.A. Porter, K.E. Easterling, Phase Transformations in Metals and Alloys, Third ed., Taylor & Francis, 1992 (Revised Reprint) <https://books.google.com/books?id=eYR5Re5tZisC>.
- [53] P. Lejček, Grain Boundary Segregation in Metals, Springer Science & Business Media, 2010.
- [54] T. Shinoda, K. Masuda-Jindo, T. Suzuki, Tight-binding calculation of the solute-dislocation interaction energy in nickel: Effect of atomic relaxation, *Philos. Mag. B* 62 (1990) 289–309, doi:10.1080/13642819008208631.
- [55] G.P.M. Leyson, W.A. Curtin, L.G. Hector, C.F. Woodward, Quantitative prediction of solute strengthening in aluminium alloys, *Nat. Mater.* 9 (2010) 750–755.